

Metric Similarity and Manifold Learning of Circular Dichroism Spectra of Proteins

Gionni Marchetti *

(Dated: April 29, 2025)

We present a machine learning analysis of circular dichroism spectra of globular proteins from the SP175 database, using the optimal transport-based 1-Wasserstein distance \mathcal{W}_1 (with order $p = 1$) and the manifold learning algorithm t -SNE. Our results demonstrate that \mathcal{W}_1 is consistent with both Euclidean and Manhattan metrics while exhibiting robustness to noise. On the other hand, t -SNE uncovers meaningful structure in the high-dimensional data. The clustering in the t -SNE embedding is primarily determined by proteins with distinct secondary structure compositions: one cluster predominantly contains β -rich proteins, while the other consists mainly of proteins with mixed α/β and α -helical content.

I. INTRODUCTION

Circular Dichroism (CD) spectroscopy is a nondestructive method for determining the secondary structure of proteins, polypeptides, and peptide structures, including their local shape, folding, and binding properties [1, 2]. Furthermore, this technique can be used to assess the self-assembly and aggregation of proteins and peptides in solution under various environmental conditions and to study intrinsically disordered proteins [3, 4]. CD spectroscopy is also advantageous due to its relatively low protein requirement and the rapid acquisition of spectral data [3, 5].

Several online resources are available for analyzing CD spectra and accurately predicting their secondary structure content (for a comprehensive list, see Ref. [6]). For instance, the BeStSel web server not only predicts the secondary structure content of proteins from their CD spectra but also offers additional functionalities, such as extinction coefficient calculation and fold recognition. In particular, the performance of BeStSel critically depends on the Cosine distance (or Cosine similarity), see Eq. 3, when applied to disorder-order classification [4, 6, 7]. Note that the Cosine distance and other “classical” similarity measures, such as the Euclidean and Manhattan metrics, can be used in spectral library search procedures to identify unknown substances [8].

Furthermore, since CD spectra live in a high-dimensional space, manifold learning (or equivalently, reduction) methods may uncover meaningful structures in lower-dimensional spaces. To this end, principal component analysis (PCA) is undoubtedly the standard choice in spectroscopy [9].

This work aims to demonstrate how CD spectral analysis can be significantly enhanced through the optimal-transport (OT) based 1-Wasserstein distance \mathcal{W}_1 of order $p = 1$ and t -distributed stochastic neighbor embedding (t -SNE) [10–12]. These two tools have recently received increased interest for their successful applications in machine learning (ML), image processing, and single-cell transcriptomics [13–15].

First, we show that the 1-Wasserstein distance aligns with the Euclidean and Manhattan similarity metrics when applied to the CD spectra of globular proteins from the reduced SP175 dataset [16] (see Section II), which contains mainly mixed α/β and β -structure rich proteins [17]. In this context, CD spectra must be mapped to suitable discrete probability density functions (probability mass functions) following OT theory, as explained in Section III. Furthermore, in contrast to the other metrics under scrutiny, the 1-Wasserstein distance is uniquely robust to additive white noise added to the spectral data. Although such a toy model of synthetic noise does not fully capture the complexities of experimental noise [18], it provides evidence that \mathcal{W}_1 is a noise-resistant distance, as observed in other fields [14].

Second, t -SNE applied to the reduced SP175 dataset reveals the existence of two distinct clusters (see Fig. 9). These clusters consist of similar instances: one is primarily composed of instances rich in β -structure, while the other predominantly contains instances with mixed α/β - and α -structures. It is worth noting that initializing t -SNE with the principal component analysis (PCA) is crucial in achieving such a meaningful embedding. This is because only with this informative initialization can t -SNE preserve both the global and local structures of the data as recently shown by Kobak and Linderman [19]. However, unlike t -SNE, PCA on its own fails to reveal any meaningful structure when applied to the same database as shown in Fig. 8. In Section V, we give a plausible explanation for this failure. It is found that PCA tends to preserve the largest pairwise Euclidean distances between spectra in high-dimensional space, so biasing the first principal component axis [20].

Finally, we conclude by noting that to identify clusters within the two-dimensional embedding, we employed the Gaussian Mixture Model (GMM), a probabilistic generative approach [21, 22]. Our choice of GMM was chiefly motivated by the observation that the clusters are not spherical. In this context, the optimal number of Gaussian components was determined using the Bayesian Information Criterion (BIC), also known as the Schwarz Information Criterion, which is considered well suited to select the true model from a set of candidates [22, 23].

* gionniamarchetti@gmail.com

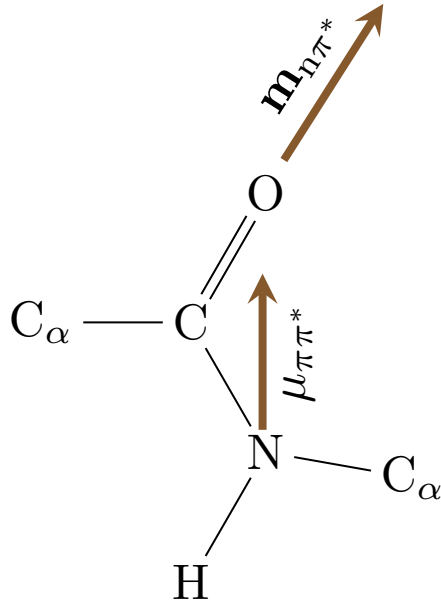


FIG. 1. The electronic transitions allowed in the amide group are the electric dipole transition moment $\mu_{\pi\pi^*}$ and the magnetic dipole transition moment $\mathbf{m}_{\pi\pi^*}$. Note that this sketch does not display the peptide-bond resonance structures.

II. CIRCULAR DICHROISM SPECTRA AND REDUCED DATASET SP175

The theory of CD applied to the proteins explains that the observed absorption bands in the far UV region are due to electronic transitions in the amide (or peptide) bond. These transitions correspond to linear and circular electronic charge motions. Precisely, quantum mechanics predicts that the electric and magnetic dipole transition moments $\mu_{\pi\pi^*}$ and $\mathbf{m}_{\pi\pi^*}$ corresponding to the electronic transitions $\pi\pi^*$ and $n\pi^*$, respectively, are non-zero at specific wavelengths [24–28]. In Fig. 1 $\mu_{\pi\pi^*}$ and $\mathbf{m}_{\pi\pi^*}$ show the directions along which the linear and helical displacement of charge, respectively, occurs in the amide group.

The CD spectra provide helpful information about the secondary structural elements of the proteins. For instance, BeStSel can predict eight secondary structure components corresponding to α -helix, β -sheets groups, turn and others [6, 29].

Next, to illustrate how the proposed methodology works, we have constructed a dataset selecting some synchrotron radiation CD spectra stored in the Protein Circular Dichroism Data Bank (PCDDB). PCDDB is a freely accessible repository [16] that also provides links to various resources, in particular to the Protein Data Bank (PDB) [30] and the AlphaFold Protein Structure Database [31, 32].

We apply our statistical learning approach to the pro-

cessed CD spectra from the SP175 dataset. This database contains 85 spectra of globular proteins, with more proteins with predominantly β and mixed α/β secondary structures than those of proteins of *alpha*-rich structure [17]. Furthermore, among the spectra in SP175, after removing some duplicates, e.g., Avidin (PDB: 1RAV) and streptavidin (PDB: 1STP), we retained only those spectra whose wavelength range could be truncated to yield the largest possible wavelength interval 175 – 279 nm. Note that the above interval comprises the far UV region 180 – 250 nm [4]. As a result, we obtained a reduced SP175 consisting of 72 spectra with $n = 105$ components, composed by 18%, 35% and 47%, of proteins with predominantly α , β , and mixed α/β secondary structures, respectively. In particular, this new dataset contains hemoglobin (PDB: 1HDA) spectra at two concentrations: 6.32 mg/ml and 7 mg/ml, respectively. In Fig. 12 of the Supplementary Information (SI) CD spectra of three specific proteins belonging to the reduced SP175 dataset are shown to illustrate the typical spectral characteristics due to a predominantly α -, mixed α/β - and β -structures.

We conclude by noting that these spectra live in \mathbb{R}^n with $n = 105$. This is a very high-dimensional space, and hence, manifold reduction algorithms are needed to investigate the data structure.

III. WASSERSTEIN DISTANCES

The Wasserstein metrics (Kantorovich-Rubinstein metrics) are distances for probability distributions or measures. They naturally arise from the optimal transport (OT) theory [10]. Originally, Monge formulated the OT problem as finding a transport map that minimizes transport cost [33]. However, this deterministic approach was later relaxed by Kantorovich, who introduced the concept of a transport plan (or coupling) [34, 35], allowing mass to be split during transport. Moreover, the OT problems solution i.e., the optimal coupling can be obtained by minimizing a linear function (see Eq. 1) subject to convex and linear constraints [36]. In the following, we briefly recall the main results of the OT problem applied to one-dimensional discrete distributions. This is particularly relevant because we will map the CD spectra to suitable discrete probability distributions, as will become clear later. Let us consider two discrete distributions $\xi = \sum_{i=1}^n \mathbf{a}_i \delta_{\lambda_i}$ (Fig. 2) and $\eta = \sum_{j=1}^m \mathbf{b}_j \delta_{\omega_j}$, where δ_{λ_i} and δ_{ω_j} are the Dirac functions at the points (or wavelengths) λ_i and ω_j in the supports of ξ and η , respectively. Accordingly, it is assumed that the components of vectors \mathbf{a} and \mathbf{b} add up to unity, i.e., $\sum_{i=1}^n a_i = 1$ and $\sum_{j=1}^m b_j = 1$. That being said, given the probability distributions ξ and η , the Kantorovich's approach requires to find a coupling \mathbf{P} among the following class of bi-stochastic matrices $\mathbf{U}(\mathbf{a}, \mathbf{b}) = \{\mathbf{P} \in \mathbb{R}_+^{n \times m} : \mathbf{P} \mathbf{1}_m = \mathbf{a} \text{ and } \mathbf{P}^T \mathbf{1}_n = \mathbf{b}\}$, by minimizing the following total cost \mathcal{L}_c [14]:

$$\mathcal{L}_c(\xi, \eta) = \min_{\mathbf{P} \in \mathbf{U}(\mathbf{a}, \mathbf{b})} \langle \mathbf{C}, \mathbf{P} \rangle, \quad (1)$$

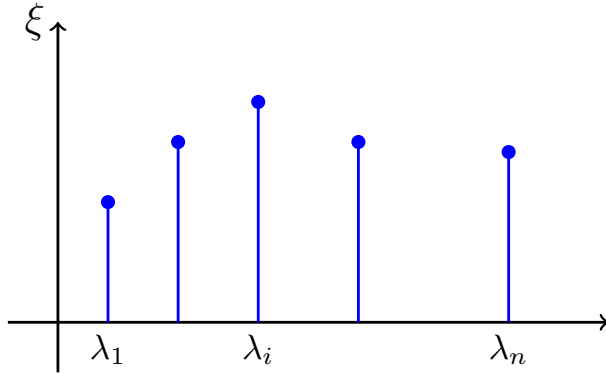


FIG. 2. Schematic stem plot representing the one-dimensional discrete distribution (probability mass) $\xi = \sum_{i=1}^n \mathbf{a}_i \delta_{\lambda_i}$ where $\mathbf{a} = (a_1, \dots, a_n)$ is a vector whose components satisfy the following constraint: $\sum_{i=1}^n a_i = 1$. The symbol δ_{λ_i} denotes the Dirac function at λ_i .

where $\langle \cdot, \cdot \rangle$ denotes the Frobenius inner product and \mathbf{C} is the cost matrix. Note that in Eq. 1 a minimum is searched, which implies that the solution always exists. However, this holds only under some conditions, e.g., the cost is continuous, and thus in general an infimum should be instead present in Eq. 1 (we refer the reader to Ref. [37] for the minimal assumptions that guarantee the existence of the solution).

In the following, we shall assume that $\mathbf{C}_{i,j} = d(\lambda_i, \omega_j)^p$ where $d = |\lambda_i - \omega_j|$ is the Euclidean distance in \mathbb{R} . Next, denoting the optimal coupling by \mathbf{P}^* for the above linear program (Eq. 1), the Wasserstein distance \mathcal{W}_p of order p ($p \geq 1$) between α and β , assuming $m = n$, is

$$\mathcal{W}_p(\xi, \eta) = (\langle \mathbf{C}, \mathbf{P}^* \rangle)^{1/p}. \quad (2)$$

The p -Wasserstein \mathcal{W}_p satisfies all the properties of a metric: the non-negativity, identity of indiscernibles, symmetry, and triangular inequality [14]. In the present work, we shall compute 1-Wasserstein \mathcal{W}_1 between spectra by mapping them to suitable probability distributions. For this purpose, all the spectral data points must be shifted by the same amount (a rigid translation by a suitable fixed constant vector) to ensure that all spectral intensities are non-negative. Subsequently, each spectrum should be normalized by dividing it by the sum of its amplitudes. The above preprocessing is routinely employed for ML analysis of Raman spectra [9]. Consequently, the support of the discrete distributions will align with the wavenumber interval of the CD spectra.

Fig. 3 (left panel) illustrates how the procedure of mapping spectra to probability masses works for the specific case of the CD spectra of Carbonic Anhydrase I (PDB: 1HCB) and Human Serum Albumin (PDB: 1N5U, concentration ≈ 4.4 mg/ml) proteins. The spectra are translated by the same amount along the vertical axis, thus making them nonnegative, and subsequently divided by the sum

of their amplitudes. We chose these two proteins because they have the largest 1-Wasserstein distance ($\mathcal{W}_1 \approx 8.11$) for the spectral data under scrutiny. This is true also for Euclidean and Manhattan distances, whose values are reported in Table I. The corresponding optimal transport plan \mathbf{P}^* solution of Eq. 2, assuming as input and target the discrete distributions associated with the spectra of 1HCB and 1N5U, is shown on the right panel of Fig. 3. The transport plan is very sparse. Its nonzero entries chiefly lie along the diagonal, and those off the diagonal correspond to the largest peaks of the input and target distributions, where the mass transport is substantial.

A. Classical Distances

The Euclidean and Manhattan (or Citiblock metric) distances are the standard similarity tools used to compare spectra through their intensities, thus ignoring their spatial information [8]. The Euclidean metric gives equal importance to each wavenumber, while the Manhattan metric is more sensitive to small differences. For two spectra whose intensities are stored in the following n -dimensional vectors $\mathbf{i} = (i_1, \dots, i_n)$ and $\mathbf{j} = (j_1, \dots, j_n)$, the Euclidean and Manhattan distances are $d = (\sum_{l=1}^n (i_l - j_l))^{{1}/{2}}$ and $d_m = \sum_{l=1}^n |i_l - j_l|$, respectively. We note that using the Euclidean norm $\|\cdot\|_2$ we can also write $d = \|\mathbf{i} - \mathbf{j}\|_2$.

Finally, the cosine distance (or cosine similarity) d_{\cos} between the spectral intensities vectors \mathbf{i} and \mathbf{j} reads [38]

$$d_{\cos}(\mathbf{i}, \mathbf{j}) = 1 - \frac{\mathbf{i} \cdot \mathbf{j}}{\|\mathbf{i}\|_2 \|\mathbf{j}\|_2}. \quad (3)$$

Note that all these “classical” similarity measures depend directly on the spectral amplitude. Furthermore, we shall use the cosine distance for t-SNE because one would expect it to make this algorithm less susceptible to the curse of dimensionality.

IV. MANIFOLD LEARNING: PCA AND T-SNE

The principal component analysis is a parametric linear unsupervised dimensionality reduction technique [39], useful for data visualization in a low-dimensional space. PCA finds new uncorrelated variables, the principal components (PCs), via a linear transformation [40, 41]. Accordingly, the axes corresponding to PCs maximally preserve the variance of high-dimensional data in decreasing order. The variances preserved (explained) along the PC axes are the eigenvalues λ_l with $l = 1, \dots, n$ of the (sample) covariance matrix $S = (n_s - 1)^{-1} X^T X$, where X^T denotes the transpose of the data matrix X [39]. In the present case, the matrix X is $n_s \times n$. However, as we shall compute the covariance matrix’s eigenvalues from the singular value decomposition (SVD), we perform the mean centering of X . Additionally, we shall scale it to

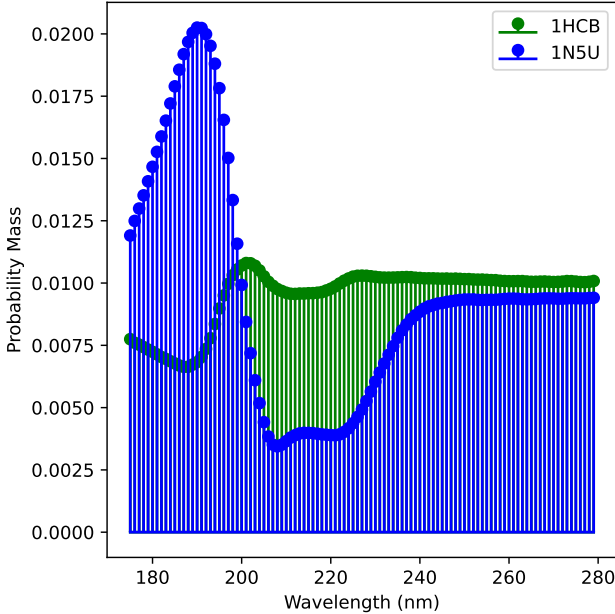


FIG. 3. The probability mass (discrete probability density function) associated with the CD spectra of Carbonic Anhydrase I (PDB: 1HCB) and Human Serum Albumin (PDB: 1N5U) proteins.

unit variance (standardization procedure) [39]. The new data matrix \tilde{X} , whose covariance matrix is again C , can be decomposed through SVD as $\tilde{X} = WLV^T$ where W and V are two suitable orthogonal matrices, and L is a diagonal matrix [39, 42, 43]. As a result, the eigenvalues λ_i can be efficiently computed from the equation $\lambda_i = (n_s - 1)^{-1} s_i^2$ where s_i are the diagonal entries of L . Furthermore, it is assumed that $s_1^2 \geq s_2^2 \geq \dots \geq s_n^2 \geq 0$. Consequently, the singular values s_i of \tilde{X} are computed from the scikit-learn ML library [44].

In contrast to PCA, t-SNE renounces preserving the pairwise distances, thereby avoiding the possible issues arising from the high dimensionality of the data. To this end, the algorithm replaces the distances between the datapoints in $\mathcal{X} = \{x_1, x_2, \dots, x_{n_s}\}$, where each element x_i belongs to \mathbb{R}^n with a symmetric joint-probability distribution P . Consequently, it searches for a low-dimensional embedding (or map) $\mathcal{Y} = \{y_1, y_2, \dots, y_{n_s}\}$, characterized by a symmetric joint-probability distribution Q , by minimizing, through the gradient descent, an objective function corresponding to the Kullback-Leibler (KL) divergence $\text{KL}(P\|Q)$ between P and Q :

$$\text{KL}(P\|Q) = \sum_{i=1}^{n_s} \sum_{j=1, j \neq i}^{n_s} p_{ij} \log \frac{p_{ij}}{q_{ij}}, \quad (4)$$

where the symmetric probabilities $p_{ij} = (2n_s)^{-1} (p_{i|j} + p_{j|i})$ and $q_{ij} = (2n_s)^{-1} (q_{i|j} + q_{j|i})$ depend on the conditional probabilities $p_{j|i}$ and $p_{i|j}$, respectively. The probabilities p_{ij} and q_{ij} measure the

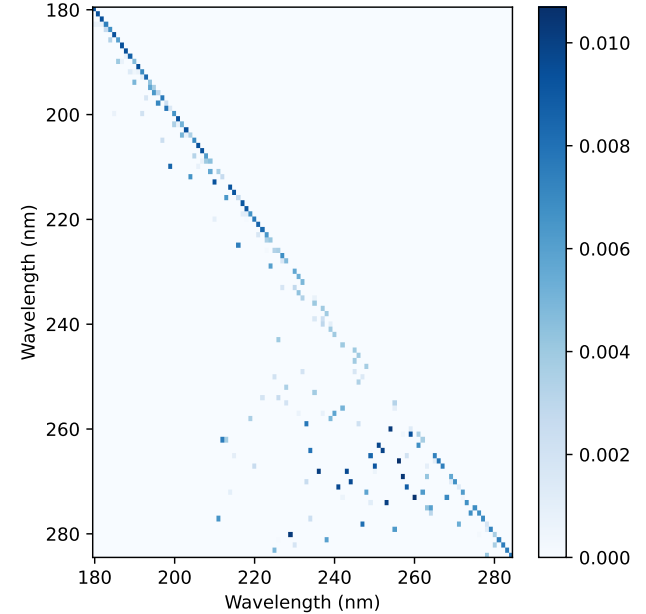


FIG. 4. The optimal transport plan (or coupling), \mathbf{P}^* solution of Eq. 2 for probability masses associated with the CD spectra of Carbonic Anhydrase I (PDB: 1HCB) and Human Serum Albumin (PDB: 1N5U) proteins.

similarity between x_i , x_j and y_i , y_j , respectively. On the other hand, $p_{j|i}$ yields the probability that x_j would be a neighbor of x_i , as a Gaussian kernel:

$$p_{j|i} = \frac{\exp(-\|x_i - x_j\|_2^2/2\sigma_i^2)}{\sum_{k=1, k \neq i}^{n_s} \exp(-\|x_i - x_k\|_2^2/2\sigma_i^2)}, \quad (5)$$

where the kernel width σ_i accounts for the local density. The variance σ_i^2 is determined by specifying the perplexity parameter τ_p . The latter is assumed to vary from 5 to 50, 30 being the default value [12?]. The perplexity can be thought of as the effective number of neighbors.

Similarly, $q_{j|i}$ yields the probability that y_j would be a neighbor of y_i . However, given a pair of datapoints belonging to \mathcal{Y} , the probability q_{ij} is now based on the t-distribution with one degree of freedom (equivalently, the Cauchy distribution), and reads

$$q_{ij} = \frac{\left(1 + \|y_i - y_j\|_2^2\right)^{-1}}{\sum_{k=1, k \neq i}^{n_s} \left(1 + \|y_k - y_i\|_2^2\right)^{-1}}. \quad (6)$$

We refer the reader to Ref. [15] for computational details about the algorithm implementation. In this work, t-SNE computations will be performed through openTSNE [45].

Finally, the Euclidean distance in Eq. ?? can be replaced by d_{cos} , which is believed to be less affected by high-dimensional data compared to the Euclidean distance. This appears to be the case in the present work, where the cosine distance performs better.

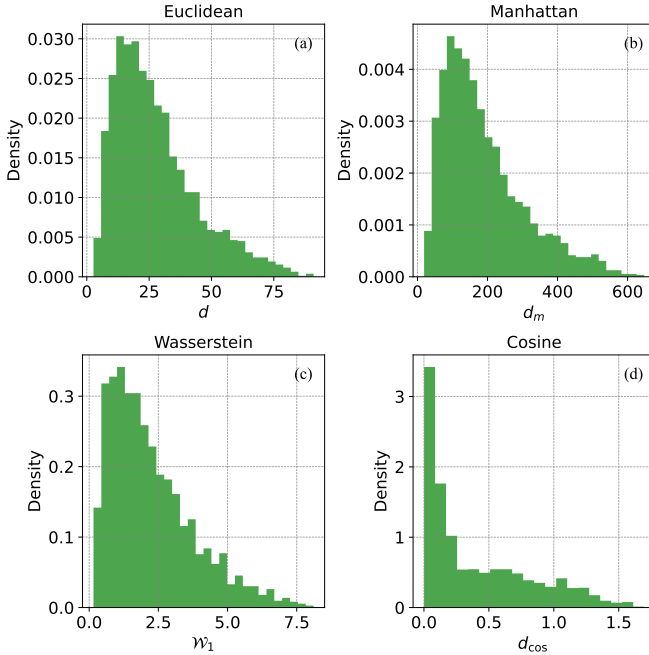


FIG. 5. Normalized histograms of the pairwise distances computed between the CD spectra of the reduced SP175 dataset. Panels (a), (b), (c), and (d) correspond to Euclidean, Manhattan, Wasserstein ($p = 1$), and Cosine distances, respectively. Each histogram consists of 2556 computed distances.

V. RESULTS AND DISCUSSION

First, we provide evidence that the Wasserstein distance ($p = 1$) is valuable for assessing the similarity between CD spectra. We find that it aligns with the Euclidean and Manhattan metrics when applied to CD spectra while also demonstrating robustness to noise. To this end, we compute all possible pairwise distances of d , d_m , \mathcal{W}_1 , and d_{\cos} for the spectra in the reduced SP175 database. The respective normalized histograms are shown in Fig. 5, and their descriptive statistics are reported in Table I.

Each histogram displays $\binom{72}{2} = 2556$ pairwise distances. All histograms are skewed to the right, leading to a positive adjusted Fisher-Pearson standardized moment coefficient G_1 (see Table I) [46]. However, the distinct shape of the Cosine distance distribution may result from the fact that, unlike the other distances, d_{\cos} is not a proper metric, as it does not satisfy the triangle inequality.

The small distances between the spectra almost certainly imply that they must be highly similar [47]. Therefore, to identify the most similar spectra in the dataset, one should search for the minimal values attained by d , d_m , \mathcal{W}_1 , and d_{\cos} . The minimal values sought are shown in Table I. Next, according to d , d_m and \mathcal{W}_1 , the two spectra of Lectin from lentil and pea sources with PDB ID: 1LES and PDB ID: 1OFS are the most similar. On the other hand, the Cosine distance indicates that the pairs of spectra of Hemoglobin and Myoglobin proteins are the

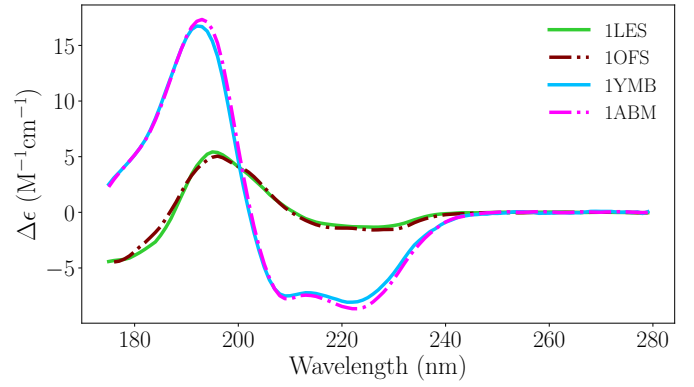


FIG. 6. The CD spectra of Lectin and Myoglobin proteins as a function of the wavelength (nm). The PDB entries are 1LES, 1OFS, 1YMB, and 1ABM, corresponding to Lectin (lentil), Lectin (pea), Myoglobin (horse), and Myoglobin (sperm whale), respectively. The symbol $\Delta\epsilon$ denotes the molar CD.

most similar ($d_{\cos} \approx 1.13 \times 10^{-3}$). To confirm that these are reasonable results, the spectra of Lectin and Myoglobin proteins, the latter with PDB ID: 1YMB and PDB ID: 1ABM, corresponding to horse and whale sources, respectively, are shown as functions of the wavelength in Fig. 6. Note that Myoglobin proteins are α -structure rich, while Lectin proteins are β -structure rich [17].

Therefore, we can conclude that the metrics under scrutiny imply that spectra with the same shape and slight amplitude differences are highly similar. However, in the context of CD spectroscopy, we must recall that spectra with similar shapes do not necessarily have the same secondary structure content. For example, CD spectra of globular proteins, rich in highly twisted antiparallel β -sheet, can hardly be distinguished from those of disordered proteins [4].

In Ref. [14], it is stated that the 1-Wasserstein distance is usually robust to outliers and noise [14]. In the following, we shall prove that \mathcal{W}_1 is indeed noise-resistant when applied to circular dichroism spectra. To this end, for simplicity, we shall model it as an additive noise that follows an independent, identically distributed Gaussian distribution with zero mean and variance, i.e. $\epsilon \sim \mathcal{N}(0, \sigma_n^2)$ [48]. This means that the amplitude components of each spectrum (i_1, \dots, i_n) will be replaced by $(i_1 + \epsilon_1, \dots, i_n + \epsilon_n)$, where the positive quantities $\epsilon_1, \dots, \epsilon_n$ are randomly sampled from $\mathcal{N}(0, \sigma_n^2)$. Note that such a synthetic noise model is an ideal approximation because the white noise does not comply with the experimental noise [18]. However, this toy model should help illustrate why \mathcal{W}_1 may be particularly advantageous if some noise is present in the CD data.

Accordingly, we generated new CD data with additive white noise by randomly sampling from $\mathcal{N}(0, \sigma_n^2)$. The choice of $\sigma_n^2 = 5$ was dictated by noting that no substantial changes were observed in the distributions of the distances for $\sigma_n^2 < 5$. By setting $\sigma_n^2 = 5$, the average signal-to-noise ratio (SNR) computed from the new data is ≈ 1.34 dB. As

TABLE I. Descriptive statistics of the data obtained by computing the pairwise distances of CD spectra of SP175, using d , d_m , \mathcal{W}_1 , and d_{\cos} . Here, Min and Max denote the minimum and maximum values attained by d , d_m , \mathcal{W}_1 , and d_{\cos} . The SD and IQR are acronyms for the standard deviation and interquartile range, respectively. The symbol G_1 is the adjusted Fisher-Pearson standardized moment coefficient.

| Metric | Min | Max | Mean | SD | Median | Mode | IQR | G_1 |
|--------------------------------|----------------------|--------|--------|--------|--------|--------|--------|-------|
| Euclidean, d | 2.68 | 90.96 | 27.67 | 16.48 | 24.04 | 23.64 | 21.00 | 1.05 |
| Manhattan, d_m | 18.87 | 647.50 | 189.24 | 117.42 | 158.74 | 158.59 | 149.08 | 1.10 |
| 1-Wasserstein, \mathcal{W}_1 | 0.15 | 8.11 | 2.25 | 1.52 | 1.88 | 1.97 | 1.98 | 1.06 |
| Cosine, d_{\cos} | 1.1×10^{-3} | 1.69 | 0.40 | 0.41 | 0.22 | 0.03 | 0.60 | 0.96 |

a consequence, there will be some spectra with more signal than noise (SNR positive) and vice versa (SNR negative) in the new spectral data. However, the corresponding normalized histograms and statistics of the computed values of all possible pairwise distances d , d_m , \mathcal{W}_1 , and d_{\cos} of these new spectral data are shown in Fig. 7 and Table II (SI), respectively.

Histograms and their statistics clearly show that noise significantly affects d , d_m , and d_{\cos} , altering either their probability distributions or their support ranges. On the other hand, noise has a negligible effect on \mathcal{W}_1 , as clearly illustrated by the overlapping histograms with and without white noise shown in Fig. 11 (SI)

Principal component analysis plays a crucial role as an informative initialization of t-SNE. Therefore, it is interesting to examine what insights it can provide on its own when applied to the reduced SP175 database.

Next, the PCA projections of datapoints belonging to the reduced SP175 dataset onto the optimal two-dimensional principal subspace are shown in Fig. 8. In such a case, it is found that the first two principal components, PC1 and PC2, approximately preserve 55.51% and 10.58%, respectively, of the total variance. In general, this amount of $\approx 66\%$, which is close enough to 70% of the explained variance, is customarily assumed when choosing how many principal components should be retained [39]. In this regard, it is found that about 20 principal components PCs are sufficient to preserve the total variance (see Fig. 13 in SI). However, despite such reasonable performance, PCA fails to recover any meaningful structure in the high-dimensional data, as shown by its projections along the PC1 and PC2 axes. For instance, some apparent outliers emerge. In particular, PCA suggests that Avidin (PDB ID: 1RAV) should be an outlier, placing it far on the left corner of the scatterplot. We note in passing that even sparse PCA (sPCA) using lasso (L_1) penalty yields a very similar embedding as shown in Fig 14 (SI) [22, 49].

We can explain the above results by noting that PCA is related to the Euclidean norm through the reconstruction error J_2 . PCA projects the datapoints onto the 2-dimensional optimal subspace by minimizing the follow-

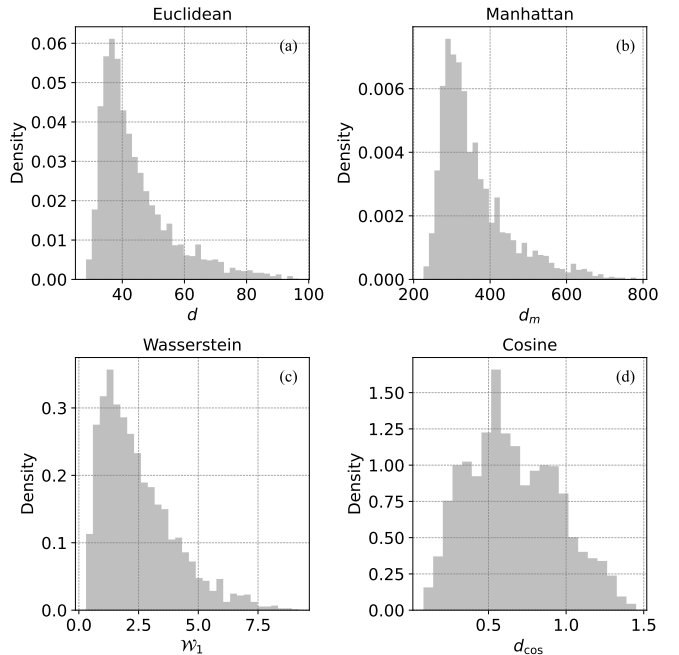


FIG. 7. Normalized histograms of the pairwise distances computed between the CD spectra in the SP175 dataset, subject to additive white noise $\mathcal{N}(0, \sigma_n^2)$ with variance $\sigma_n^2 = 5$. Panels (a), (b), (c), and (d) correspond to Euclidean, Manhattan, Wasserstein ($p = 1$), and Cosine distance, respectively. Each dataset consists of 2556 computed distances.

ing reconstruction error $J_2 = n_s^{-1} \sum_{j=1}^{n_s} \|x_j - y_j\|_2^2$ [50] [51]. Therefore, PCA strongly depends on the Euclidean distances between the datapoints in the high-dimensional space. Their overall effect on PCA can be inferred by distribution shown on panel (a) of Fig. 5. Because this distribution is skewed, there does not exist a typical Euclidean distance, corresponding to either the mean or the median, which are appropriate measures of the central tendency [52]. As a result, PCA is misled by directions in which the distances are large [20]. To confirm this observation, we note that the largest Euclidean distance

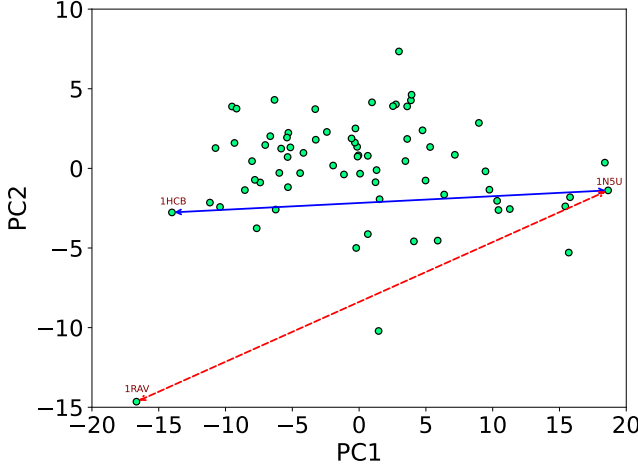


FIG. 8. The two-dimensional optimal principal subspace where the reduced SP175 dataset is projected along the PC1 and PC2 axes. The (blue) solid and (red) dotted lines connect the datapoints corresponding to the spectra with the largest Euclidean and Manhattan distances in \mathbb{R}^{105} , respectively. The PDB entries 1HCB, 1N5U, and 1RAV correspond to Carbonic Anhydrase I, Human Serum Albumin (HSA), and Avidin, respectively.

≈ 90.96 , occurs between Carbonic Anhydrase I (PDB entry: 1HCB) and Human Serum Albumin (PDB entry: 1N5U). In Fig. 8, their two-dimensional projections are shown joined by a blue line, which approximates their original distance in \mathbb{R}^{105} . The PC1 axis is almost aligned with this blue line. As a result, PCA becomes biased, obscuring the true data structure and instead producing noticeable artifacts (outliers).

Next, we show how the actual data structure can be recovered by *t*-SNE. This algorithm is applied to the reduced SP175 dataset by keeping all optimization parameters at their default values, e.g., the algorithm was run with the regular early exaggeration phase 12 for 250 iterations, then in normal regime with no exaggeration for 500 iterations [45]. PCA is used for initialization. The perplexity τ_p is set to 23 for the calculations presented here. This choice is motivated by the observation that, around this value, the instances grouped by the *t*-SNE embedding into two distinct clusters represented in yellow and blue for clearer visualization in Fig. 9 remain stable under further tuning of τ_p . Note that the *t*-SNE embedding was obtained using the cosine distance, which is commonly considered less susceptible to the curse of dimensionality. On the other hand, *t*-SNE embeddings with Euclidean distance cannot displace the clusters apart; see, for instance, Fig. 15 (SI) where the same perplexity parameter was used, i.e. $\tau_p = 23$. More generally, it is found that *t*-SNE with the Euclidean metric makes it more challenging to automatically determine the appropriate number of clusters n_c as discussed below within the Bayesian information criterion applied to the Gaussian Mixture model.

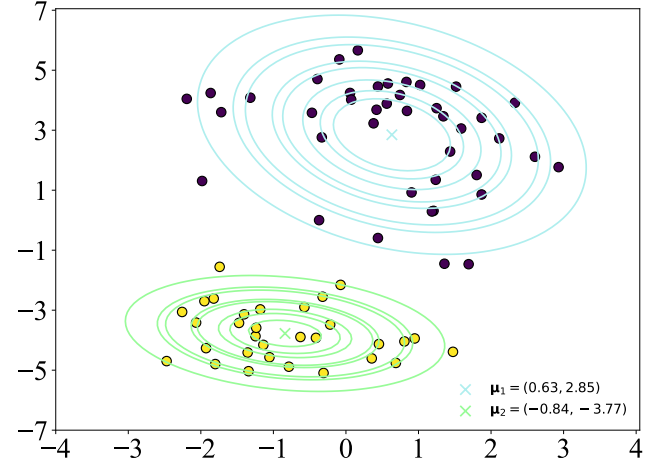


FIG. 9. The two-dimensional embedding of the reduced SP175 dataset using *t*-SNE with the cosine distance d_{\cos} , and assuming $\tau_p = 23$. PCA was used for initializing the algorithm. The instances are assigned to two clusters according to GMM ($n_c = 2$). The contour lines correspond to Gaussians with mean vectors μ_1 and μ_2 , and covariance matrices Σ_1 and Σ_2 given in Eq. 9.

Upon inspection, it is found that the lower (yellow circles) and upper (blue circles) clusters are mainly composed of instances corresponding to β -rich and α -rich/mixed α/β proteins, respectively. In particular, the bottom and top clusters group approximately 98% and 100% of the β -sheet- and α -helical-rich proteins from the reduced SP175 dataset, respectively.

To address the clustering problem rigorously, we resort to BIC applied to GMM [21, 22]. Within the GMM, the choice of n_c , which corresponds to the number of components that form the Gaussian mixture model, can be based on the Bayesian information criterion by fitting the GMM to the embedding data, maximizing the log-likelihood. The BIC reads [22]:

$$\text{BIC} = (\log n_s) n_f - 2 \log \hat{L}, \quad (7)$$

where n_f is the number of independent parameters and $\log \hat{L}$ is the maximized value of the likelihood function of the model in question. On the right-hand side of Eq. 7, the first term accounts for the model complexity, and the second term measures how well the model fits the data. Note that BIC penalizes models with high complexity. The optimal number of clusters is expected to be the minimum reached by BIC when n_c varies as shown in Fig. 10. There is a minimum at $n_c = 2$, which further supports what is shown in Fig. 9. Note that the computations of GMM for a given n_c were carried out ensuring that the expectation-maximization (EM) algorithm is converged [44, 53]. Furthermore, it is worth noting here that for $n_c = 2$, $n_f = 11$ due to the contributions of the parameters determining the two-component GMM: the mixture weights ϕ_m , mean vectors μ_m and covariance

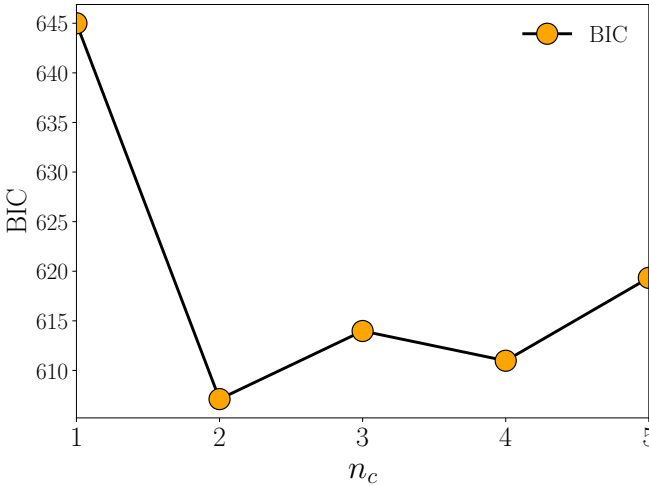


FIG. 10. BIC as function of the number of clusters n_c . Each BIC value is obtained by fitting the respective GMM to t -SNE’s two-dimensional embedding \mathcal{Y} of the reduced SP175 dataset, using cosine distance, $\tau_p = 23$, and PCA initialization, then computing Eq. 7.

matrices Σ_m ($m = 1, 2$) (see Eq. 8). In contrast, the BIC criterion predicts the existence of a unique cluster in the t -SNE embedding \mathcal{Y} , obtained using the Euclidean distance, see Fig. 16 (SI). In such a case, the minimum occurs at $n_c = 1$. This finding suggests that the cosine distance is more suitable for dealing with the curse of dimensionality in the present case.

That being said, we can now fit the GMM with two components to the data. Accordingly, the Gaussian mixture model has the form [22]

$$f(y) = \sum_{m=1}^2 \phi_m g(y; \boldsymbol{\mu}_m, \Sigma_m), \quad (8)$$

where g is the Gaussian density. Note that the weights ϕ_1 and ϕ_2 must add up to unity. The fit obtained through the EM convergence yields the following numerical estimates: $\phi_1 \approx 0.57$, $\phi_2 \approx 0.43$, $\boldsymbol{\mu}_1 = (0.63, 2.85)$, $\boldsymbol{\mu}_2 = (-0.84, -3.77)$, and:

$$\Sigma_1 = \begin{bmatrix} 1.49 & -0.61 \\ -0.61 & 3.30 \end{bmatrix}, \quad \Sigma_2 = \begin{bmatrix} 1.02 & -0.19 \\ -0.19 & 0.78 \end{bmatrix}. \quad (9)$$

With these parameters learned, the GMM assigned each instance to the most likely cluster, as illustrated by plotting the contour lines of the two Gaussian densities in Fig. 9.

We conclude by noting that the mixture weights agree with those obtained using a Bayesian approach to GMM [53]. The latter yields the following Bayesian weights: $\phi_1^B \approx 0.54$, $\phi_2^B \approx 0.46$.

VI. CONCLUSION

We demonstrated that some state-of-the-art machine learning tools can meaningfully analyze proteins’ circular dichroism spectra. First, the 1-Wasserstein metric can successfully replace classical similarity measures, such as the Euclidean and Manhattan distances, which rely solely on intensity differences. Due to its robustness to noise, \mathcal{W}_1 outperforms these classical metrics. Interestingly, other transport-based distances, such as TL^p distance [54], could also be considered as alternatives to \mathcal{W}_1 . In such cases, the fact that CD spectra are not strictly positive does not pose a problem.

Second, in contrast to PCA, t -SNE can help reveal clustering based on the type of secondary structure that characterizes the CD spectra. However, it is crucial to initialize it using PCA, as this step allows the manifold learning algorithm to preserve both the global and local structure of the high-dimensional data.

Remarkably, both methods presented here are probabilistic. The stochastic neighbor embedding t -SNE interprets the pairwise distances between the data points as symmetric probabilities. At the same time, \mathcal{W}_1 arises from the change in perspective from Monge’s formulation of the transport problem, as a one-to-one mapping (deterministic transport) to Kantorovich’s relaxation, which allows for probability distributions (probabilistic transport).

Finally, even though these methods are applied to circular dichroism spectra, they can also be successfully employed for analyzing the spectra of another type, such as UV resonance Raman and UV-Vis absorption spectra [55–58].

Acknowledgements

The author thanks A. B. Wallace for helpful information regarding the SP175 dataset, and Alessio Figalli and Gabriel Peyré for their correspondence on the Wasserstein metric.

Data Availability

The data used in this article can be downloaded from the PCDDDB public repository for circular dichroism spectral data (<https://pcddb.cryst.bbk.ac.uk/>).

[1] N. J. Greenfield, Using circular dichroism spectra to estimate protein secondary structure, *Nature Protocols* **1**,

2876 (2006).

- [2] L. Whitmore and B. A. Wallace, Protein secondary structure analyses from circular dichroism spectroscopy: Methods and reference databases, *Biopolymers* **89**, 392 (2008).
- [3] M. F. Pignataro, M. G. Herrera, and V. I. Dodero, Evaluation of peptide/protein self-assembly and aggregation by spectroscopic methods, *Molecules* **25** (2020).
- [4] A. Micsonai, É. Moussong, N. Murvai, Á. Tantos, O. Tke, M. Réfrégiers, F. Wien, and J. Kardos, Disordered protein binary classification by circular dichroism spectroscopy, *Frontiers in Molecular Biosciences* **9** (2022).
- [5] J. T. Pelton and L. R. McLean, Spectroscopic methods for analysis of protein secondary structure, *Analytical Biochemistry* **277**, 167 (2000).
- [6] A. Micsonai, . Moussong, F. Wien, E. Boros, H. Vadszi, N. Murvai, Y.-H. Lee, T. Molnr, M. Rfrgiers, Y. Goto, . Tantos, and J. Kardos, Bestsel: webserver for secondary structure and fold prediction for protein cd spectroscopy, *Nucleic Acids Research* **50**, W90 (2022).
- [7] A. Micsonai, F. Wien, É. Bulyáki, J. Kun, É. Moussong, Y.-H. Lee, Y. Goto, M. Réfrégiers, and J. Kardos, Bestsel: a web server for accurate protein secondary structure prediction and fold recognition from the circular dichroism spectra, *Nucleic Acids Research* **46**, W315 (2018).
- [8] S. S. Khan and M. G. Madden, New similarity metrics for raman spectroscopy, *Chemometrics and Intelligent Laboratory Systems* **114**, 99 (2012).
- [9] G. Shuxia, J. Popp, and T. Bocklitz, Chemometric analysis in raman spectroscopy from experimental design to machine learning-based modeling, *Nature Protocols* **16**, 5426 (2021).
- [10] C. Villani, *Optimal Transport. Old and New* (Springer Berlin, Heildeberg, 2008).
- [11] G. E. Hinton and S. T. Roweis, Stochastic neighbor embedding, in *Neural Information Processing Systems* (2002).
- [12] L. van der Maaten and G. Hinton, Visualizing data using t-sne, *Journal of Machine Learning Research* **9**, 2579 (2008).
- [13] S. Kolouri, S. R. Park, M. Thorpe, D. Slepcev, and G. K. Rohde, Optimal mass transport: Signal processing and machine-learning applications, *IEEE Signal Processing Magazine* **34**, 43 (2017).
- [14] G. Peyr and M. Cuturi, Computational optimal transport (2020), [arXiv:1803.00567 \[stat.ML\]](https://arxiv.org/abs/1803.00567).
- [15] D. Kobak and P. Berens, The art of using t-sne for single-cell transcriptomics, *Nature Communications* **10**, 5416 (2019).
- [16] S. G. Ramalli, A. J. Miles, R. W. Janes, and B. Wallace, The pcdbs (protein circular dichroism data bank): A bioinformatics resource for protein characterisations and methods development, *Journal of Molecular Biology* **434**, 167441 (2022), computation Resources for Molecular Biology.
- [17] J. G. Lees, A. J. Miles, F. Wien, and B. A. Wallace, A reference database for circular dichroism spectroscopy covering fold and secondary structure space, *Bioinformatics* **22**, 1955 (2006).
- [18] S. E. F. Spencer and A. Rodger, Bayesian inference assessment of protein secondary structure analysis using circular dichroism data how much structural information is contained in protein circular dichroism spectra?, *Anal. Methods* **13**, 359 (2021).
- [19] D. Kobak and G. C. Linderman, Initialization is critical for preserving global data structure in both t-sne and umap, *Nature Biotechnology* **39**, 156 (2021).
- [20] M. Greenacre, P. J. F. Groenen, T. Hastie, A. I. DEnza, A. I. Markos, and E. Tuzhilina, Principal component analysis, *Nature Reviews Methods Primers* **2** (2022).
- [21] A. Lindholm, N. Wahlström, F. Lindsten, and T. Schön, *Machine Learning: A First Course for Engineers and Scientists* (Cambridge University Press, 2022).
- [22] T. J. Hastie, J. H. Friedman, and R. Tibshirani, *Springer Series in Statistics*, 2nd ed. (Springer, 2020).
- [23] G. Schwarz, Estimating the dimension of a model, *Annals of Statistics* **6**, 461 (1978).
- [24] W. Moffitt, Optical rotatory dispersion of helical polymers, *The Journal of Chemical Physics* **25**, 467 (1956).
- [25] I. Tinoco Jr., Theoretical aspects of optical activity part two: Polymers, in *Advances in Chemical Physics* (John Wiley & Sons, Ltd, 1962) pp. 113–160.
- [26] B. M. Bulheller, A. Rodger, and J. D. Hirst, Circular and linear dichroism of proteins, *Phys. Chem. Chem. Phys.* **9**, 2020 (2007).
- [27] R. W. Woody, The circular dichroism of oriented beta sheets: Theoretical predictions, *Tetrahedron: Asymmetry* **4**, 529 (1993).
- [28] G. D. Fasman, Circular dichroism and the conformational analysis of biomolecules, in *Springer US* (1996).
- [29] W. Kabsch and C. Sander, Dictionary of protein secondary structure: Pattern recognition of hydrogen-bonded and geometrical features, *Biopolymers* **22**, 2577 (1983).
- [30] S. K. Burley, C. Bhikadiya, C. Bi, S. Bitrich, L. Chen, G. V. Crichlow, C. H. Christie, K. Dalenberg, L. Di Costanzo, J. M. Duarte, S. Dutta, Z. Feng, S. Ganesan, D. S. Goodsell, S. Ghosh, R. K. Green, V. Guranovi, D. Guzenko, B. P. Hudson, C. Lawson, Y. Liang, R. Lowe, H. Namkoong, E. Peisach, I. Persikova, C. Randle, A. Rose, Y. Rose, A. Sali, J. Segura, M. Sekharan, C. Shao, Y.-P. Tao, M. Voigt, J. Westbrook, J. Y. Young, C. Zardecki, and M. Zhuravleva, Rcsb protein data bank: powerful new tools for exploring 3d structures of biological macromolecules for basic and applied research and education in fundamental biology, biomedicine, biotechnology, bioengineering and energy sciences, *Nucleic Acids Research* **49**, D437 (2020), <https://academic.oup.com/nar/article-pdf/49/D1/D437/35364241/gkaa1038.pdf>.
- [31] J. Jumper, R. Evans, A. Pritzel, T. Green, M. Figurnov, O. Ronneberger, K. Tunyasuvunakool, R. Bates, A. Žídek, A. Potapenko, A. Bridgland, C. Meyer, S. A. A. Kohl, A. J. Ballard, A. Cowie, B. Romera-Paredes, S. Nikolov, R. Jain, J. Adler, T. Back, S. Petersen, D. Reiman, E. Clancy, M. Zielinski, M. Steinegger, M. Pacholska, T. Berghammer, S. Bodenstein, D. Silver, O. Vinyals, A. W. Senior, K. Kavukcuoglu, P. Kohli, and D. Hassabis, Highly accurate protein structure prediction with alphafold, *Nature* **596**, 583 (2021).
- [32] M. Varadi, S. Anyango, M. Deshpande, S. Nair, C. Natasia, G. Yordanova, D. Yuan, O. Stroe, G. Wood, A. Laydon, A. dek, T. Green, K. Tunyasuvunakool, S. Petersen, J. Jumper, E. Clancy, R. Green, A. Vora, M. Lutfi, M. Figurnov, A. Cowie, N. Hobbs, P. Kohli, G. Klewegt, E. Birney, D. Hassabis, and S. Velankar, Alphafold protein structure database: massively expanding the structural coverage of protein-sequence space with high-accuracy models, *Nucleic Acids Research* **50**, D439 (2021), <https://academic.oup.com/nar/article-pdf/50/D1/D439/43502749/gkab1061.pdf>.

- [33] G. Monge, Mémoire sur la théorie des déblais et des remblais, De l'Imprimerie Royale (1781).
- [34] L. V. Kantorovich, A problem of monge, *Uspekhi Mat. Nauk* **3**(24):225–226 (1948).
- [35] L. V. Kantorovich, Mathematical methods of organizing and planning production, *Management Science* **6**(4):366–422 (1960).
- [36] A. Figalli and F. Glaudo, *An Invitation to Optimal Transport, Wasserstein Distances, and Gradient Flows* (EMS Press, 2021).
- [37] F. Santambrogio, *Optimal Transport for Applied Mathematicians* (Springer International Publishing, Switzerland, 2015).
- [38] K. P. Murphy, *Machine learning - a probabilistic perspective* (MIT Press, Cambridge, Massachusetts, 2012).
- [39] I. T. Jolliffe and J. Cadima, Principal component analysis: a review and recent developments, *Philosophical Transactions of the Royal Society A: Mathematical, Physical and Engineering Sciences* **374**, 20150202 (2016).
- [40] K. Pearson, On lines and planes of closest fit to systems of points in space, *Philosophical Magazine Series 1* **2**, 559 (1901).
- [41] H. Hotelling, Analysis of a complex of statistical variables into principal components., *Journal of Educational Psychology* **24**, 498 (1933).
- [42] G. Strang, The fundamental theorem of linear algebra, *The American Mathematical Monthly* **100**, 848 (1993).
- [43] G. W. Stewart, On the early history of the singular value decomposition, *SIAM Review* **35**, 551 (1993).
- [44] F. Pedregosa, G. Varoquaux, A. Gramfort, V. Michel, B. Thirion, O. Grisel, M. Blondel, P. Prettenhofer, R. Weiss, V. Dubourg, J. Vanderplas, A. Passos, D. Cournapeau, M. Brucher, M. Perrot, and Édouard Duchesnay, Scikit-learn: Machine learning in python, *Journal of Machine Learning Research* **12**, 2825 (2011).
- [45] P. G. Poliar, M. Straar, and B. Zupan, opentsne: A modular python library for t-sne dimensionality reduction and embedding, *Journal of Statistical Software* **109**, 130 (2024).
- [46] D. P. Doane and L. E. Seward, Measuring skewness: A forgotten statistic?, *Journal of Statistics Education* **19** (2011).
- [47] J. Delaporte, B. M. Herbst, W. A. Hereman, and V. der Walt Stéfan, An introduction to diffusion maps, in *Proceedings of the 19th symposium of the pattern recognition association of South Africa (PRASA 2008)* (Cape Town, South Africa, 2008) pp. 15–25.
- [48] C. E. Rasmussen and K. I. Williams, *Gaussian Processes for Machine Learning* (MIT Press, 2006).
- [49] H. Zou, T. Hastie, and R. Tibshirani, Sparse principal component analysis, *Journal of Computational and Graphical Statistics* **15**, 265 (2006).
- [50] M. P. Deisenroth, A. A. Faisal, and C. S. Ong, *Mathematics for Machine Learning* (Cambridge University Press, 2020).
- [51] In this context, the reconstruction error can be directly computed via the correlation matrix's eigenvalues through $J_2 = \sum_{l=3}^n \lambda_l$.
- [52] D. Spiegelhalter, *The Art of Statistics. Learning from Data* (Penguin Random House UK, 2020).
- [53] A. Géron, *Hands-On Machine Learning with Scikit-Learn and TensorFlow: Concepts, Tools, and Techniques to Build Intelligent Systems* (O'Reilly, U.S.A, 2019).
- [54] M. Thorpe, S. Park, S. Kolouri, G. K. Rohde, and D. Slepcev, A transportation 1 distance for signal analysis, *Journal of Mathematical Imaging and Vision* **59**, 187 (2017).
- [55] S. A. Asher, M. Ludwig, and C. R. Johnson, Uv resonance raman excitation profiles of the aromatic amino acids, *Journal of the American Chemical Society* **108**, 3186 (1986).
- [56] S. A. Oladepo, K. Xiong, Z. Hong, S. A. Asher, J. Handen, and I. K. Lednev, Uv resonance raman investigations of peptide and protein structure and dynamics, *Chemical reviews* **112**, 2604 (2012).
- [57] D. K. Asamoto and J. E. Kim, Uv resonance raman spectroscopy as a tool to probe membrane protein structure and dynamics, in *Lipid-Protein Interactions* (Springer, 2019) pp. 327–349.
- [58] S. Krimm and J. Bandekar, Vibrational spectroscopy and conformation of peptides, polypeptides, and proteins, *Advances in protein chemistry* **38**, 181 (1986).

TABLE II. Descriptive statistics of the data obtained by computing the pairwise distances of CD spectra of the reduced SP175, with additive white noise $\mathcal{N}(0, \sigma_n^2 = 5)$, using d, d_m, \mathcal{W}_1 , and d_{\cos} . Here, Min and Max denote the minimum and maximum values taken by d, d_m, \mathcal{W}_1 , and d_{\cos} . The SD and IQR are acronyms for the standard deviation and interquartile range, respectively. The symbol G_3 is the adjusted Fisher-Pearson standardized moment coefficient.

| Metric | Min | Max | Mean | SD | Median | Mode | IQR | G_3 |
|--------------------------------|--------|--------|--------|-------|--------|--------|-------|-------|
| Euclidean, d | 28.34 | 96.77 | 44.37 | 11.82 | 40.71 | 41.30 | 12.87 | 1.52 |
| Manhattan, d_m | 225.72 | 781.98 | 358.23 | 91.21 | 330.28 | 337.60 | 99.99 | 1.49 |
| 1-Wasserstein, \mathcal{W}_1 | 0.30 | 9.20 | 2.49 | 1.55 | 2.1 | 1.99 | 2.01 | 1.13 |
| Cosine, d_{\cos} | 0.081 | 1.45 | 0.66 | 0.29 | 0.62 | 0.42 | 0.43 | 0.32 |

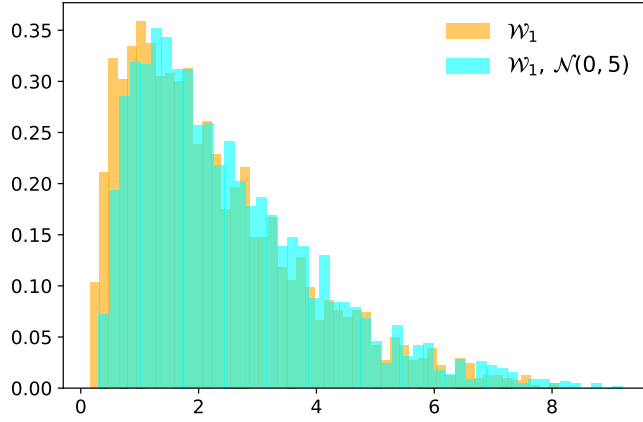


FIG. 11. Normalized histograms of the pairwise 1-Wasserstein distances computed between the CD spectra of the reduced SP175 dataset, with and without white noise. The additive white noise $\mathcal{N}(0, \sigma_n^2)$ has variance $\sigma_n^2 = 5$. Each dataset consists of 2556 computed distances.

SUPPLEMENTARY INFORMATION

The fit of GMM with $n_c = 2$ to the t-SNE embedding data \mathcal{Y} obtained using the Euclidean distance, $\tau_p = 23$ and PCA as initialization, after EM convergence, yields the following numerical estimates: $\phi_1 \approx 0.62$, $\phi_2 \approx 0.38$, $\boldsymbol{\mu}_1 = (-1.27, -2.18)$, $\boldsymbol{\mu}_2 = (2.09, 3.57)$, and:

$$\boldsymbol{\Sigma}_1 = \begin{bmatrix} 3.18 & 2.37 \\ 2.37 & 5.47 \end{bmatrix}, \quad \boldsymbol{\Sigma}_2 = \begin{bmatrix} 1.75 & -0.64 \\ -0.64 & 2.57 \end{bmatrix}. \quad (10)$$

The learned GMM assigned the instances to their respective cluster, as illustrated in Fig. 15. However, this time the top cluster (yellow circles) contains fewer β -rich proteins. It is found that there are 84% of this type.

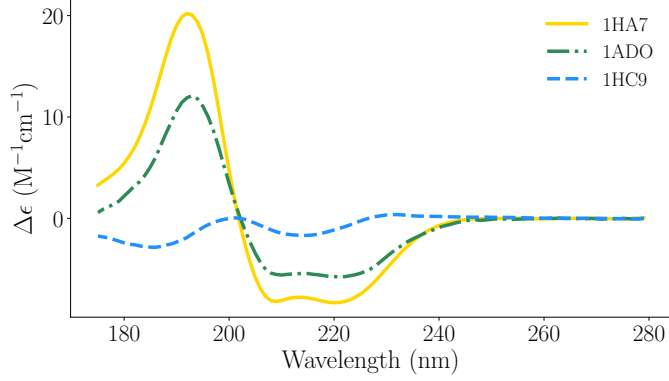


FIG. 12. The CD spectra of C-Phycocyanin (PD ID: 1HA7), Aldolase (PD ID: 1ADO) and α -Bungarotoxin (PD ID: 1HC9) proteins from the reduced SP175 dataset as functions of the wavelength. These proteins are classified as predominantly α -, mixed α/β - and β -structures.

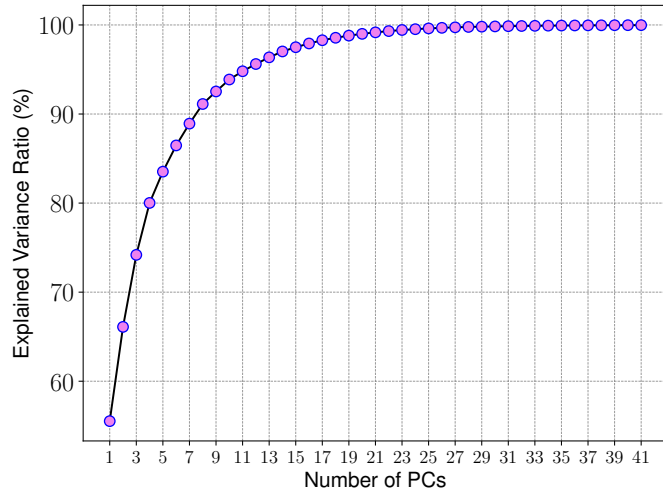


FIG. 13. Explained variance ratio in percentage as function of the first 41 principal components (PCs). Here, PCA was applied to the reduced SP175 dataset.

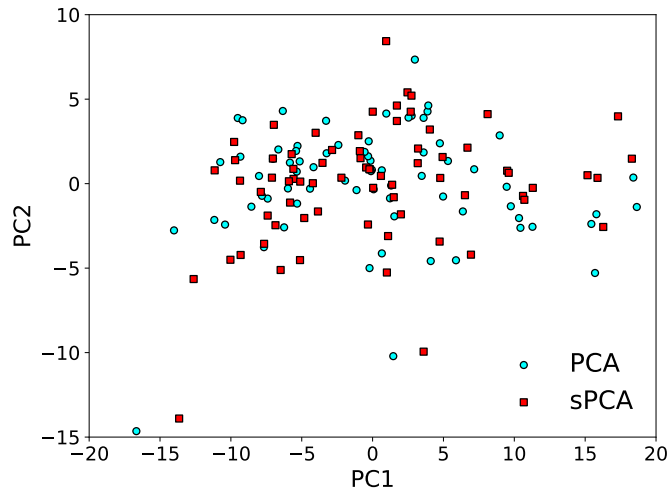


FIG. 14. The principal component analysis (PCA) (cyan circle symbols) and sparse PCA (sPCA) (red square symbols) projections of the reduced SP175 dataset using the first two principal components PC1 and PC2 axes. According to sPCA, PC1 and PC2 axes are not necessarily orthogonal.

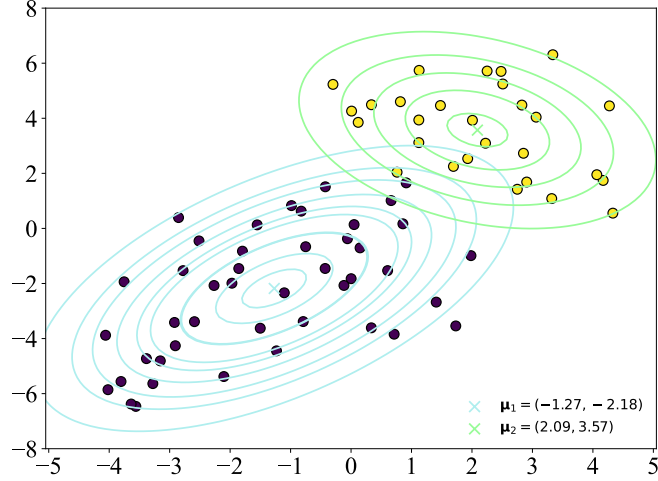


FIG. 15. The two-dimensional embedding of the reduced SP175 dataset using t-SNE with the Euclidean distance d , and assuming $\tau_p = 23$. PCA was used for initializing the algorithm. The instances are assigned to two clusters according to GMM ($n_c = 2$). The contour lines correspond to Gaussians with mean vectors μ_1 and μ_2 , and covariance matrices Σ_1 and Σ_2 given in Eq. 10.

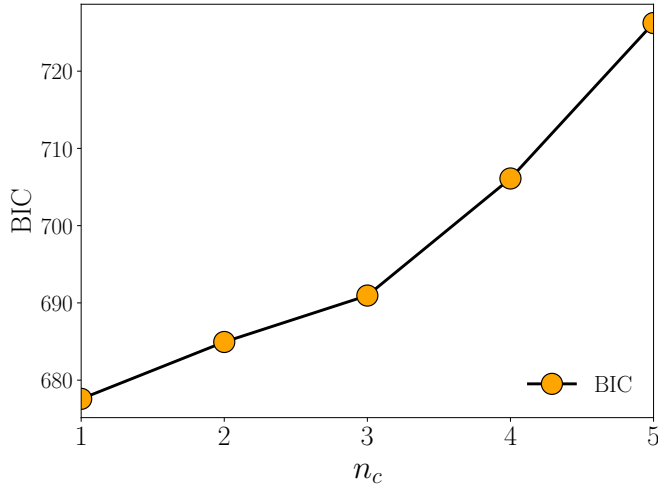


FIG. 16. BIC as function of the number of clusters n_c . Each BIC value is obtained by fitting the respective GMM to t-SNE's two-dimensional embedding \mathcal{Y} of the reduced SP175 dataset, using Euclidean distance, $\tau_p = 23$, and PCA initialization, then computing Eq. 7.